Accepted Manuscript

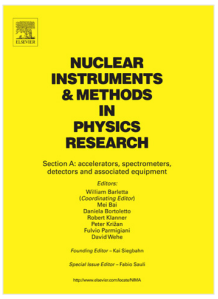

Characterisation of a small electrode HPGe detector

C. Unsworth, A.J. Boston, H.C. Boston, L.J. Harkness-Brennan, D.S. Judson, P.J. Nolan, O.S. Thomas, J.P. Wright, A.S. Adekola, J. Colaresi, W.F. Mueller, J. Simpson

PII: S0168-9002(19)30231-1
DOI: https://doi.org/10.1016/j.nima.2019.02.043
Reference: NIMA 61916

To appear in: *Nuclear Inst. and Methods in Physics Research, A*

Received date : 25 November 2018
Revised date : 15 February 2019
Accepted date : 16 February 2019

Please cite this article as: C. Unsworth, A.J. Boston, H.C. Boston et al., Characterisation of a small electrode HPGe detector, *Nuclear Inst. and Methods in Physics Research, A* (2019), https://doi.org/10.1016/j.nima.2019.02.043

Characterisation of a Small Electrode HPGe Detector

C. Unsworth, A.J. Boston, H.C. Boston, L.J. Harkness-Brennan, D.S. Judson, P.J. Nolan, O.S. Thomas, J.P. Wright

Oliver Lodge Laboratory, University of Liverpool, Liverpool, L69 7ZE, UK

A.S. Adekola, J. Colaresi, W.F. Mueller

Mirion Technologies Canberra, 800 Research Parkway, Meriden, CT, 06450, USA

J. Simpson

STFC Daresbury Laboratory, Daresbury, Warrington, WA4 4AD, UK

Abstract

Small electrode HPGe detectors in an inverted coaxial geometry are increasingly in use in applications where both high efficiency and excellent energy resolution are required. The unusual electric field configuration of these detectors results in extremely long charge collection times compared to planar and coaxial devices. In this work we have characterised such a detector using gamma-ray coincidence measurements and optimised an electric field simulation to reproduce the position dependent variation of detector response. We show that, alongside accurate crystal geometry and applied electric potential, a temperature correction is crucial to correctly determining appropriate charge carrier mobility parameters. This work will help to guide the future development of HPGE detectors for applications including radioactive waste assay, radio-isotope dating, and fundamental nuclear physics.

Keywords: HPGe, SAGe Well, Charge collection, Charge carrier mobility

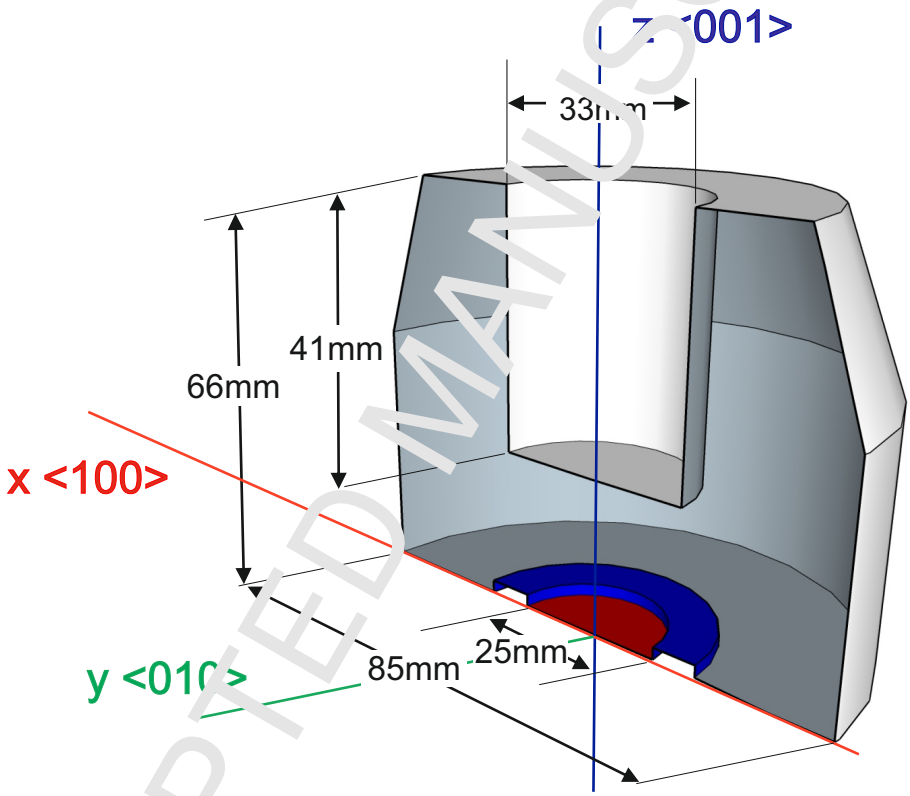

Figure 1: Schematic of the SAGe Well HPGe crystal used in this work sliced along the x axis (red). The y and z axes are shown in green and blue respectively. The 25 mm diameter p+ electrode surface is shown on the back face of the crystal in red and the passivated region surrounding it in blue, the n+ electrode covers the remaining surface of the crystal including the inside of the well. The front face of the crystal is tapered in towards the well in order to eliminate regions of very low electric field, which would otherwise lead to significant charge trapping.

1. Introduction

High-resolution gamma-ray spectrometry is used across a range of applications. These include a number of fields where both high efficiency and excellent energy resolution are critical to performance. In applications such as environmental measurements, where sample sizes are often limited, a well geometry is often used to maximise efficiency. The Small Anode Germanium (SAGe) Well [1, 2, 3] is a p-type high-purity germanium (HPGe) detector manufactured by Mirion Technologies Canberra and designed to have excellent energy resolution and very high efficiency for gamma-rays emitted by samples placed within the well.

The induced charge signals due to gamma-ray interactions at a range of positions within a SAGe Well detector have been investigated in order to characterise the charge collection behaviour. Electric field simulations and experimental measurements have been used for the characterisation with the latter being used to validate and optimise the former. The optimised field simulations can be used to predict the characteristics of other similar detectors and aid in the design of future devices.

In this work we have used a SAGe Well with a diameter of 85 mm and a length of 66 mm (*Fig. 1*). The crystal has a 33 mm diameter well bored into the front face to a depth of 41 mm and a 26 mm taper which reduces the diameter of the crystal to 65 mm at the front. These features help to reduce regions of extremely low field, which would otherwise lead to significant charge trapping. A small p+ electrode of 25 mm diameter is separated by a passivated region from the n+ electrode covering the rest of the crystal surface. The operating bias of -4700 V was applied to the p+ electrode. Relative to other detector geometries of similar volume, the small size of the p+ electrode provides reduced capacitance and hence electronic noise. This reduced noise helps the detector achieve outstanding energy resolution with FWHM of 0.73 keV at 122 keV and

*Corresponding author

1.69 keV at 1332 keV. The detector was mechanically cooled by a CP5-plus cryo cooler which allows the device to be operated in any orientation, a fact which facilitated our characterisation measurements.

Points in the detector are described by a Cartesian coordinate system with the xy plane coincident with the back face of the detector and the z axis running through the centre of the crystal towards the front face. The origin is in the centre of the p+ electrode and the x, y, z axes run parallel to the <100>, <010>, and <001> crystal axes respectively (See *Fig. 1*).

2. Simulation

Signal formation in the detector was simulated using the AGATA Data Library (ADL) [4] which was adapted for this work to incorporate the SAGe Well geometry. The simulation uses a finite difference method to solve the electric and weighting fields in the detector before tracking holes and electrons through the field using the mobility parameterisation described in [5]. The charge trajectories are then used to calculate the signal induced on an electrode using the Shockley-Ramo theorum [6, 7]. The detector was initially modelled according to the nominal geometric and material specification and using the electron and hole mobility parameters described in [8]. Optimisations of the simulation parameters to match the experimental signals are described in *Sec. 6*.

Fig 2 shows a slice of the calculated electric potential in cylindrical polar coordinates (rz with r in the xy plane), the electron and hole trajectories for each of the example signals we will be considering are also shown (See *Sec. 5* and *Fig. 4* for the equivalent experimental signals). Due to rotational symmetry of the detector this potential is the same regardless of the angle in the xy plane at which the slice is taken. The unusual field distribution in the volume surrounding the well causes the electrons (dashed blue lines) to follow the potential gradient towards the closest part of the n+ electrode while the holes approach the potential "valley" partway ($r \approx 28$ mm) between the outer detector wall and inside of the well. The holes then drift through this valley along the <001>

Position	x (mm)	y (mm)	z (mm)
R1	-9.5	0.5	13.5
R2	-14.5	0.5	13.5
R3 / D1	-27.5	0.5	13.5
R4	-36.5	0.5	13.5
D2	-27.5	0.5	30.0
D3	-27.5	0.5	46.5
D4	-27.5	0.5	62.0

Table 1: Coordinates in the detector frame of positions R1 - R4 and D1 - D4

crystal axis with the trajectories from each position converging onto a single path as they approach the p+ electrode. Holes produced by interactions anywhere in the region surrounding the well, which represents the majority of the detector volume, follow a similar path as they approach the p+ electrode.

Fig. 3 shows the weighting potential for the p+ electrode together with the same charge trajectories shown on the electric potential. The weighting potential is close to zero throughout most of the detector volume until it begins to rise quickly in the vicinity the p+ electrode ($z < 20$ mm). Together these potentials result in a range of signal shapes depending on the position of interaction in the detector. For illustrative purposes we will consider signals produced due to interactions in positions R1-4 and D1-4, the coordinates for each of these interaction positions is shown in *Table 1.* Note that points R3 and D1 are the same.

The combination of converging hole trajectories and a weighting potential concentrated close to the p+ electrode gives rise to the important features of the signal shapes from positions D1 to D4 (see *Fig. 4*). Electrons are collected quickly over a short distance while holes have a long drift with very little induced signal, then a significant induced signal as the holes approach the electrode which has a fixed shape regardless of initial interaction position.

This behaviour results in charge drift times increasing with distance from the

electrode in both the radial and z directions. Longer collection times are seen when the charge has to drift further along the common path in the z direction, or further in the radial direction before reaching the common path.

Considering the signals from the set of interaction positions R1-R4 (*Fig. 4*), on a line through the detector radius at a fixed z of 3.5 mm. Signals from positions R1 and R2, closest to the p+ electrode, have very fast (<250 ns) almost linear rising edges. Referring again to the simulated electric potential, *Fig. 2*, we see that this region of the detector has straight electric field lines with a roughly linear change in potential between the p+ electrode and the bottom of the well. Electron and hole drift distances are comparable and the charge trajectories for R1 and R2 differ only in that R2 approaches the p+ electrode at a slightly greater angle, resulting in a slightly greater rise time. Holes still make the dominant contribution to the induced signal, due to the weighting potential for the p+ electrode changing more quickly close to the electrode, but electrons do play a significant role here unlike elsewhere in the detector.

As the radius of the interaction position increases to positions R3 and R4 we see a return to behaviour seen in the well walls with electrons playing little part in the induced signal and the holes converging onto the same common trajectory before approaching the electrode.

3. Experimental Metnodology

The University of Liverpool detector characterisation system, *Fig. 5*, consists of a 1 GBq ^{137}Cs source mounted inside a lead and tungsten collimation assembly. The tungsten collimator is 160 mm long with an outer diameter of 10 mm and a 1 mm diameter hole, this sits inside an array of lead blocks. The xy position uncertainty produced by the collimator in this measurement varied from 1.2 mm diameter at the front of the detector to 2.2 mm at the back. The entire assembly is mounted on top of a pair of linear stepper motors allowing it to be moved in two dimensions to a precision of 0.1 mm.

This scan table is combined with a fully digital data acquisition system

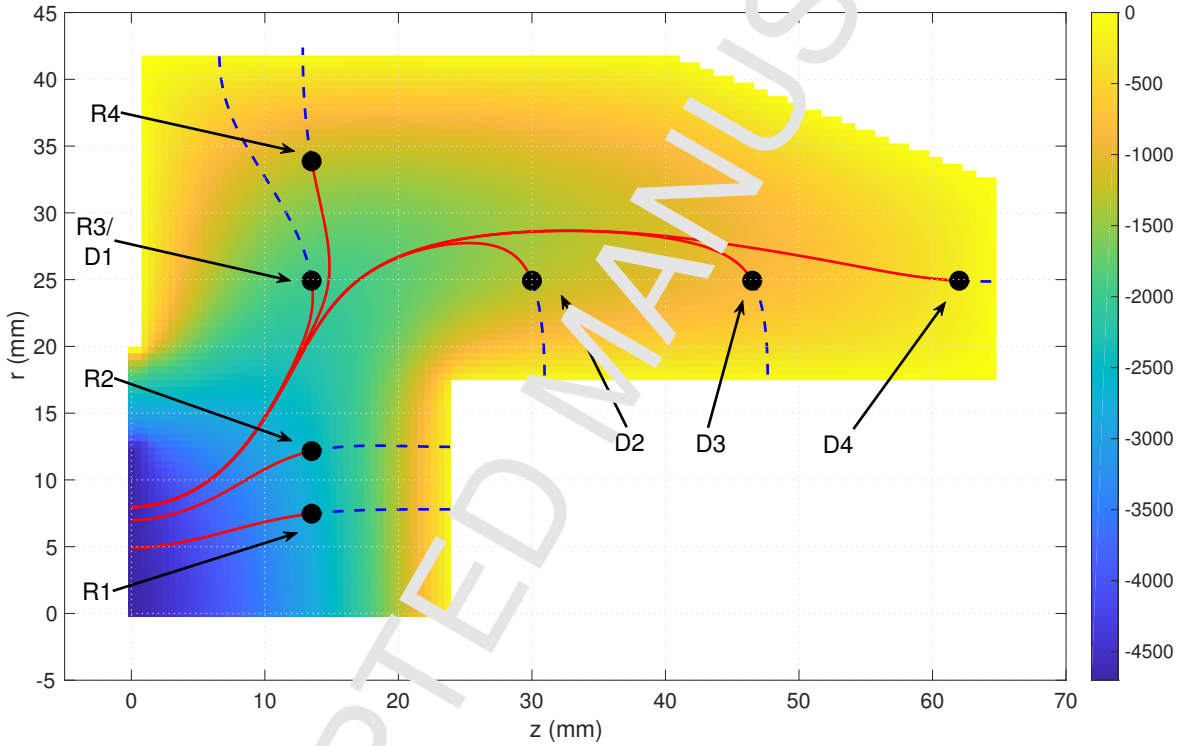

Figure 2: An rz slice of the electric potential (Volts) calculated by ADL for the SAGe Well detector, due to rotational symmetry of the detector this is the same for a slice taken at any angle in the xy plane. Electron (dashed blue) and hole (red) trajectories are shown for the seven example positions discussed in the text, the simulated interaction positions are marked with black circles.

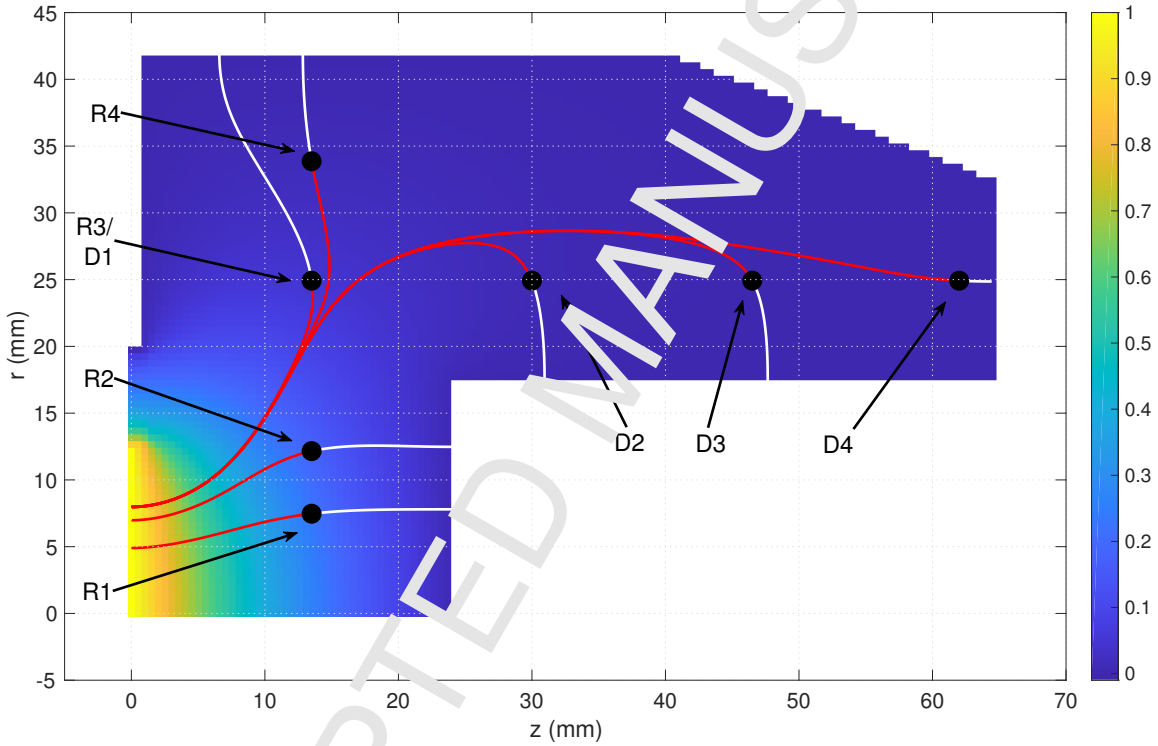

Figure 3: An rz slice of the weighting potential calculated by ADL for the SAGe Well detector p+ electrode, due to rotational symmetry of the detector this is the same for a slice taken at any angle in the xy plane. Electron (white) and hole (red) trajectories are shown for the seven example interaction positions discussed in the text, the simulated interaction positions are marked with black circles.

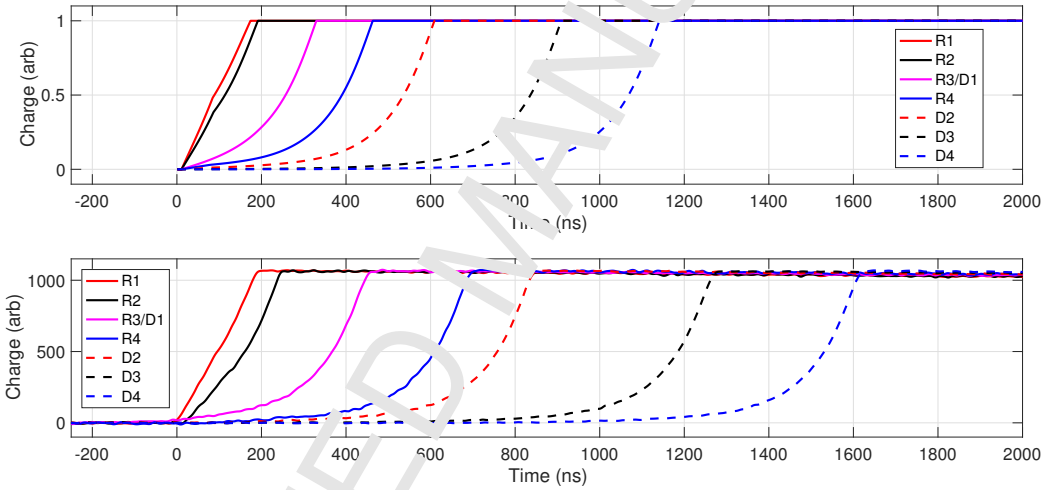

Figure 4: The top panel shows simulated signals for selected positions in the detector using the nominal detector parameters and previously published values for hole and electron mobility, see *Sec. 2*. The bottom panel shows the experimental mean signals measured during the coincidence scan for the same positions, see *Sec 3*. See *Fig. 2* and *Fig. 7* for the corresponding interaction locations

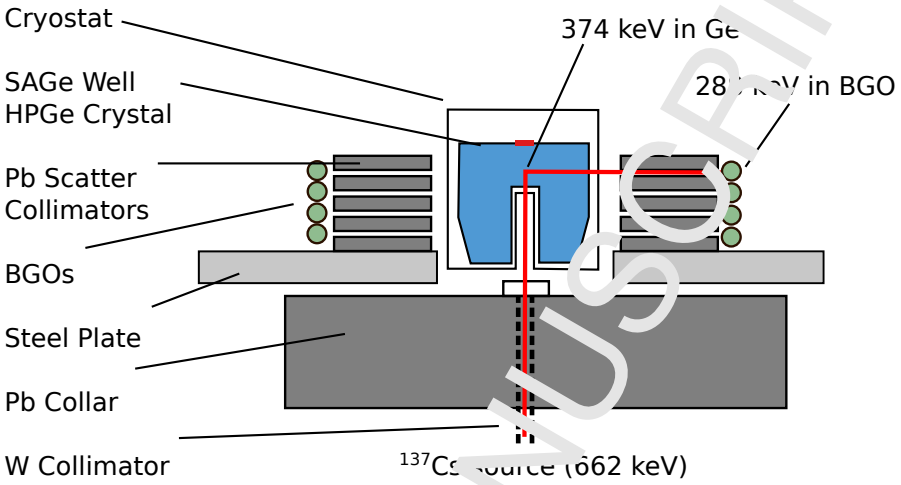

Figure 5: A schematic of the University of Liverpool Detector Scanning Table mounted with a SAGe Well detector in coincidence mode. The source, primary collimator and lead collar are moved by the stepper motors while the rest remains stationary. The red line indicates an example path of a valid coincidence event gamma-ray Compton scatter.

using Caen V1724 100 MHz 14 bit digitisers to capture detector charge signals. This system allows the positional response of a detector to be investigated by interrogating it with the beam of 662 keV gamma rays[9]. The rate of gamma rays coming from the collimator is ≈1000 per second.

The scanning system can be operated in two modes, *singles* and *coincidence*. In singles scanning mode the collimator is raster scanned across the whole of the detector with the only spatial information coming from the position of the collimator when an interaction occurs. This allows identification of the xy position of the *first* interaction undergone by a gamma ray. This method does not allow location of the interaction in the z direction nor does it provide any constraint upon the total number of interactions undergone before the full energy is deposited. Despite these limitations the singles scan data are crucial to establishing the shape, position, and orientation of the detector crystal in the frame of the scanning system.

The coincidence scan method uses in addition a secondary array of collimating lead blocks with a thickness of 80 mm and 1.5 mm gaps created by

plastic spacers. The gaps are aligned with BGO scintillation detectors which identify gamma rays that Compton scatter through 90° at defined z positions and subsequently interact in one of the BGO detectors. The geometry of the secondary collimators and detectors resulted in a z position uncertainty from 2 mm at large radii of interaction to 3 mm near the centre of the detector. The triggering electronics were configured to read out all events in which interactions occurred in both SAGe Well and BGO detectors within a coincidence window of 2 μs to cover the observed range of rise times in the detector.

Combining the information from the secondary detector with the collimator position allows the full three dimensional localisation of *single-site* interactions. If a number of signals are collected from each position it is possible to form a mean signal and hence deconvolve the underlying detector response from the random electronic noise. The rate of such coincident interactions varies with position but is typically less than one event per minute compared with a random coincidence trigger rate of the order of 100 events per minute. This necessitates the use of offline event selection techniques to identify the events of interest.

Conservation of energy and momentum ensures that for a fixed gamma-ray energy a scatter through 90° will deposit a fixed energy in each of the primary and secondary detectors. In the case of 662 keV gamma rays the values are 374 keV in the HPGe and 288 keV in the BGO. *Fig. 6* shows a plot of the BGO energy versus the HPGe energy for events measured in time coincidence. The events of interest can then be selected and the background reduced with gates on both energies as shown in the figure. The width of the gates applied depends on both the collimator geometry and the energy resolution of the detectors, in this measurement our gates were 374 ± 12 keV in the HPGe and 288 ± 40 keV in the BGO. Prominent lines in the background of *Fig. 6* represent the 662 keV photopeak and 511 keV annihilation photons in the germanium with random background events in the BGO. Further background suppression can be achieved by limiting the Ge-BGO time difference to a range of values consistent with being due to the scattering of a single gamma ray. See *Sec. 5* for further discussion of the Ge and BGO time difference.

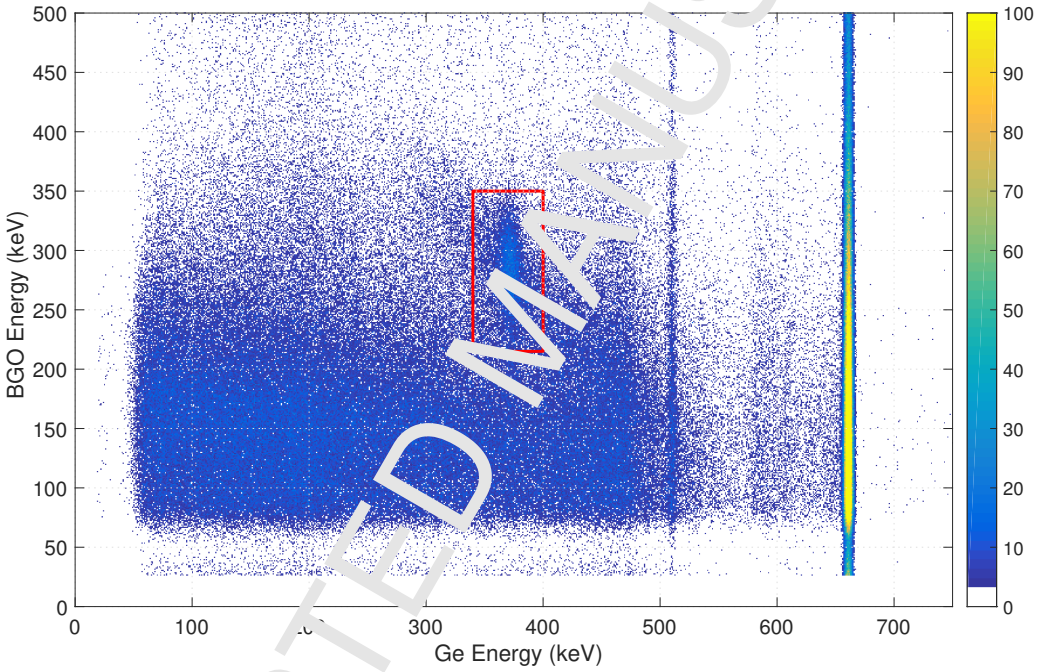

Figure 6: Energy deposited in HPGe and in BGO during the SAGe Well scan. The feature marked by the red box represents Compton scattering through 90° leaving 374 keV in the germanium and 28[illegible] keV in one of the BGO detectors. Prominent vertical lines represent the 66[illegible] keV photopeak and 511 keV annihilation photons in the germanium with random background events in the BGO.

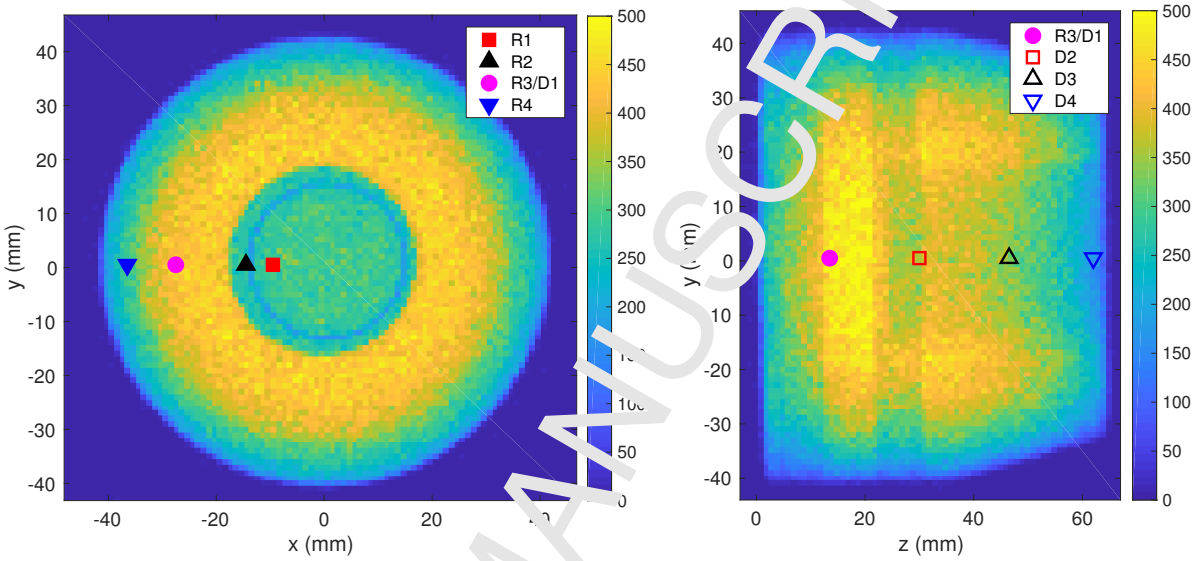

Figure 7: 662 keV photopeak counts as a function of position for the front (left) and side (right) scans. The coordinates have been translated into the detector frame where the origin is in the centre of the p+ electrode and the x, y, and z axes run parallel to the <100>, <010>, and <001> crystal axes respectively. Example points from the coincidence scan, discussed in *Sec. 5* are indicated.

Following the application of initial time and energy gates the signals are interpolated linearly between the measured points at 10 ns intervals down to 2 ns samples. They are then shifted in time to align the point where they reach 10% of their maximum to a fixed sample number and normalised to equal height before an initial mean signal for this position is formed. The final stage of filtering is to compare each individual signal to this initial mean and measure the RMS difference between the two, signals with large differences are rejected and a final mean signal is formed from those that remain.

4. Singles Scan Results

Fig. 7 shows the positional variation of 662±2 keV photopeak counts observed when the SAGe Well detector was scanned with the collimated ^{137}Cs

source. The left image shows a scan from the front of the detector and the right shows a scan from the side, in both cases the collimator was held at each position for 4 seconds. The most probable way for a 662 keV photon to leave its full energy in germanium is by first Compton scattering and then leaving its remaining energy at another location through photoelectric absorption. This results in a reduction in photopeak counts at the detector edges in both scans as the probability of the photon scattering out of the sensitive volume before depositing its full energy increases.

The well in the centre of the detector is visible in both scans as a reduction in intensity because there is less sensitive germanium material present in the path of the gamma-ray beam. Other regions of reduced intensity are the result of gamma rays interacting with attenuating material before they reach the detector. See for example the thin ring in the centre of the front scan, a consequence of scattering in the walls of the cryostat endcap, and bands of reduced intensity in the side scan, caused by the material used to physically support the crystal.

Also indicated on *Fig. 7* are the interaction locations for the example signals that will be discussed in *Sec. 5*. Points R1 to R4 lie on a radial line relatively close to the p+ electrode at z = 13.5mm. Points D1 to D4 lie at a fixed radial position on a line through the depth of the detector and parallel to the z axis.

5. Coincidence Scan Results

In the coincidence measurement the first parameter to be studied was the time difference between the signals measured in the SAGe and BGO detectors. The left side of *Fig. 8* shows the time difference between triggers generated in the both detectors during the coincidence scan for all x and y at each z positions, the black line shows all events generating a trigger and the coloured lines show the events selected for mean signal formation at each value of z. On the right side time difference for two BGOs triggered by coincident 511 keV gamma rays from a ^{22}Na source is shown, this distribution has a FWHM of 23±2 ns.

The BGO detectors generated consistent signal shapes which were not de-

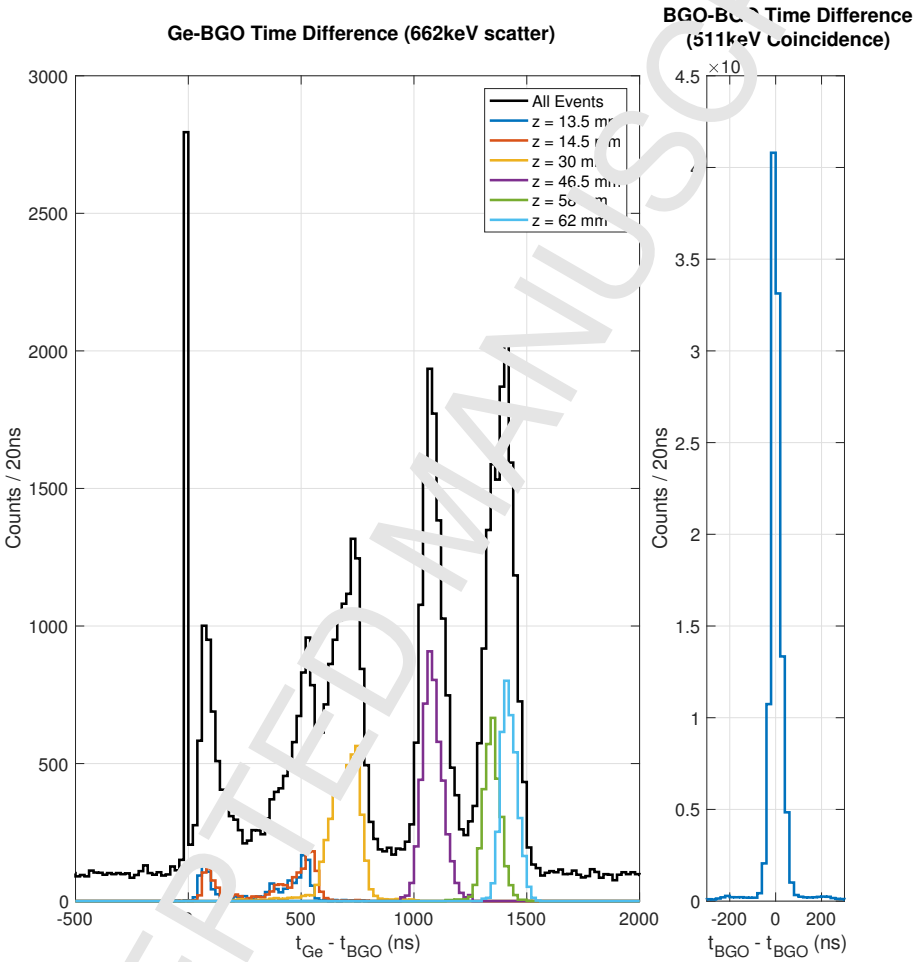

Figure 8: Histograms of the SAGe-BGO time difference obtained during the coincidence scan (left). The black line represents all events generating a coincidence trigger, the coloured lines represent signals passing all gates and being used to form mean signals. The BGO-BGO timing response to 511 keV anhilalation photons from a ^{22}Na source is provided for comparison (right), the FWHM of this distribution was 23ns.

pendent on the position of interaction. We therefore assume any variation in the SAGE-BGO trigger time difference greater than the BGO resolution to be due to variation in the SAGe response. This distribution reveals the large range of charge collection times observed in the SAGe detector, with total collection time increasing with increasing distance from the p+ electrode up to a maximum of 1.6 μs for events near to the detector front face.

The signals in the SAGe detector will now be investigated for a range of different positions within the detector. For each mean signal formed *Fig. 9* shows the rise time for the initial (*left*) and final (*centre*) parts of the pulse (2% to 30% and 30% to 98% of its height respectively). Also shown is the mean Ge-BGO trigger time difference for events contributing to a mean signal (*right*), as a function of the position of interaction. The x axis shows the radius of the interaction position and the colour and shape of the markers indicate the z position.

The rise time of the initial part of the rising edge shows little variation through most of the detector volume as shown by the clustering of events around 400 ns. However there is a strong dependence on radius for events occurring at z positions closer to the p+ electrode, with shorter rise times seen at smaller radii. The final part of the rising edge again shows little variation through most of the detector volume but has a slight dependence on z for events close to the p+ electrode. The SAGe-BGO time differences on the other hand reveal a strong dependence on z of the time before a trigger signal is generated by the SAGe detector.

These data support the simulated charge collection behaviour described in *Sec. 2*, holes produced by a gamma-ray interaction will drift a long way through the detector before inducing any significant signal on the collecting electrode.

The mean signals produced by the method described in *Sec. 3* are aligned relative to the SAGe detector trigger time, in order to reveal the true variation in charge collection time it is necessary to shift them according to the mean SAGe - BGO time differences of the contributing signals. This method produces mean signals with the correct shape and timing relative to the BGO signal as shown

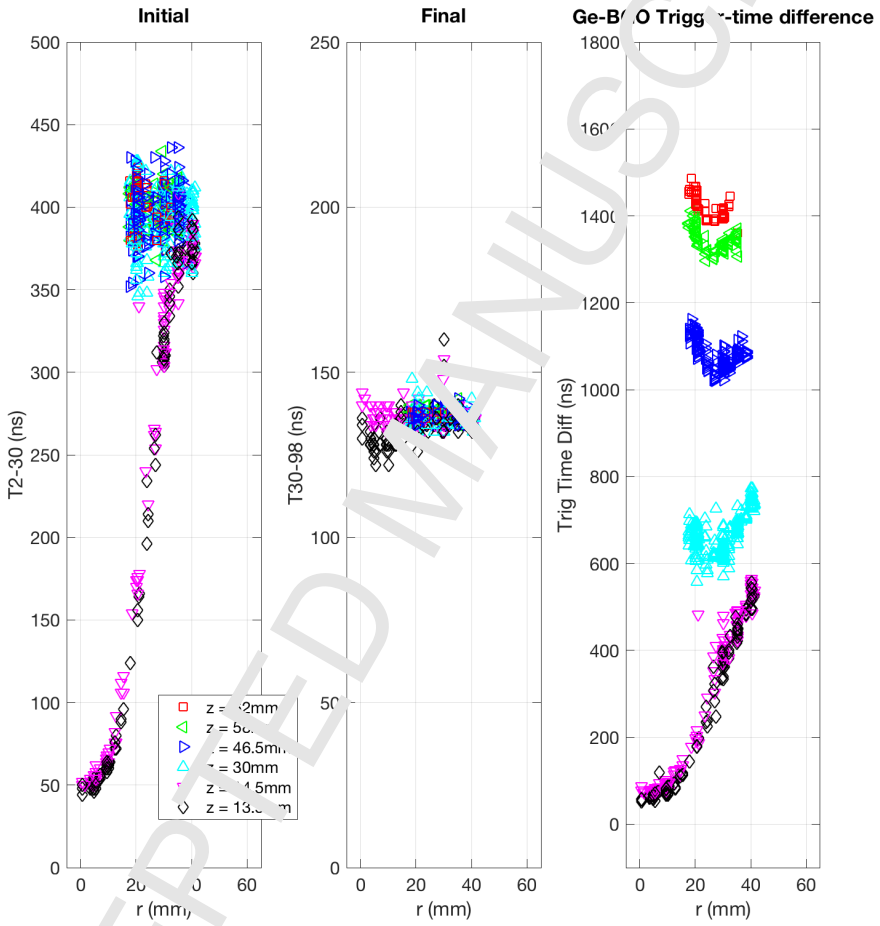

Figure 9: Shape parameters for signals induced in SAGE detector as a function of position. Time taken for mean signals to go from 2% to 30% of their height (left), from 30% to 98% of their height (centre), and the mean Ge-BGO trigger time difference (right) for events contributing to the mean signal at each position. The x axis indicates the radial position of each mean signal, the z position is indicated by the colour and marker type.

in *Fig. 4* for the example signals R1 to R4 and D1 to D4.

6. Investigating Parameters of the Simulation

Fig. 4 shows the experimental mean signals discussed in *Sec. 5* together with simulated signals for the same positions. The simulated signals show qualitatively the same behaviour, with fast rising signals for interactions close to the p+ electrode and increasing charge drift time as distance from the electrode increases.

The total charge collection times for the simulated signals are however much shorter than seen in experiment. For example, charge collection for an interaction at point D4 located at $z = 6$ mm takes 1.1 μs compared with 1.6 μs in experiment. In particular the initial part of charge collection, where charge carriers are far from the p+ electrode and the induced signal is close to zero, is significantly faster in the simulation.

Broadly, the rate of charge collection is determined by the electric field in the detector and the mobility of charge carriers being collected. The electric field at each point in the detector is determined by the detector crystal geometry, the potential at the electrodes, and the internal electric field due to stationary space charge. Details of the geometry were checked against the intensity profiles obtained through singles scanning (see *Fig. 7*) and while this measurement revealed slightly smaller dimensions than the specification the discrepancy can be explained by the existence of surface dead layers which are not visible in the scan.

Impurity concentrations were quoted by the manufacturer to within 10% at the front and back of the crystal, a linear gradient along the z axis was assumed between these points and no radial variation was included in the model. A linear in purity gradient along the z axis results in a uniform field in the bulk of the detector where the field due to space charge dominates the overall electric field. The linear variation of charge collection time as a function of z, seen in *Figs 8 and 9 (right)* supports the hypothesis of an impurity gradient which is

approximately linear in z. We were not able to determine if there is any variation in impurity concentration with xy, but any such variation would be expected to contribute mainly to the field in the xy plane and would not therefore explain the rate of charge collection along the z direction.

In order to establish if uncertainties in the impurity measurements at each end of the crystal could explain the observed charge collection times we ran the simulations again while shifting the front and back impurity concentrations by up to 20%. *Fig. 10* shows the results of these simulations for the induced signal from interactions at point D4. While there is a significant change in charge collection time, the maximum effect of a 20% shift is only enough to increase the charge collection time to 1.2 μs, still significantly less than the 1.6 μs seen in experiment.

We thus conclude that realistic uncertainties in the crystal impurity concentration are not enough to explain the observed discrepancy in charge collection times.

The hole and electron mobility parameters used for the initial simulation were obtained by a fit to experimental data from the MINIBALL array of coaxial HPGe detectors, described in *Ref [8]*. These values have had success in simulating the signal shapes generated in coaxial HPGe detectors from the AGATA array [10]. While alternative parametrisations of charge carrier mobility have produced different values [11], comparisons with data from coaxial HPGe detectors have shown relatively little sensitivity of simulation performance to choice mobility parameter [12, 13].

Ref [8] does not give the temperature of the HPGe crystals when the study was performed but the liquid-nitrogen-cooled MINIBALL and AGATA crystals typically vary between temperatures of 95 K and 100 K under normal conditions [14]. The temperature of the SAGe crystal in this study was 113 K, a value which was chosen in manufacture to optimise energy resolution. Since this difference is relatively large, and the temperature dependence of mobility is stronger in weaker electric fields, a significant temperature correction will be required here.

In order to establish if the longer charge collection times seen in experiment

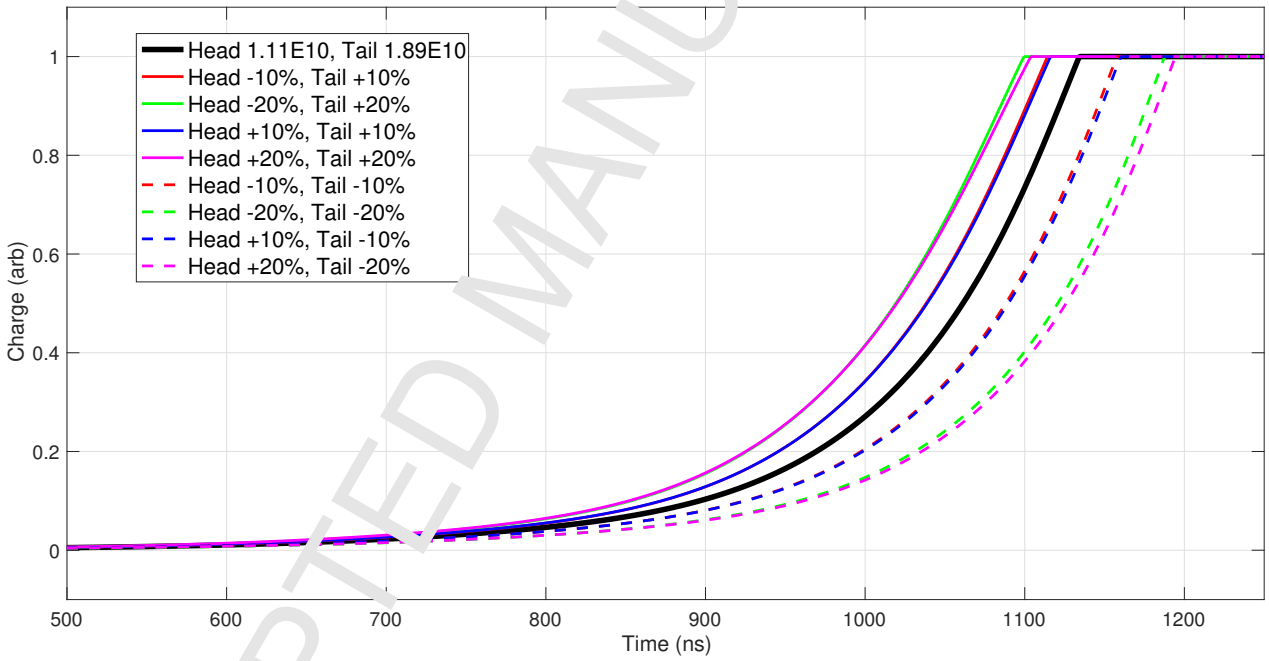

Figure 10: Simulated signals from point D4 using a range of values for the impurity concentration at the head (front) and tail (back) of the detector.

could be due to this temperature difference we ran a series of simulations with adjusted mobility parameters. As the charge collection time in the SAGe Well is dominated by the hole mobility these signals show little sensitivity to electron mobility. As such we focussed this study on hole mobilities only. The difference between experiment and simulation was most pronounced for interaction positions with the longest drift distances so we used exclusively point D4, near the front face of the detector, for this comparison.

Studies on the relationship between mobility and temperature for germanium found a dependence on $T^{-1.6}$ for electrons and $T^{-2.3}$ for holes [15, 16]. This dependence equates to a reduction in hole mobility of 33% when temperature increases from 95 K to 113 K.

Fig. 11 shows the simulated signals where the hole mobilities along the <100> and <111> axes were both changed by between +10% and -35%. The simulated signal with -30% hole mobility provides a good match to experiment for both the total charge collection time (≈1.6 μs) and the time for the signal to reach 10% of its height (≈1.3 μs). It is therefore reasonable to conclude that the crystal temperature differences are the dominant factor in the longer charge collection times seen in this SAGe well detector. With suitable temperature corrections there is excellent agreement between simulated signals and those observed in this detector.

This underlines the importance of temperature corrections to mobility for accurate simulation of signal shapes, a point which is likely of increased importance given the proliferation of inverted-coaxial type detectors with relatively weak fields [17, 18]. Furthermore, the increasing popularity of mechanically cooled detectors which may be expected to have a wider range of crystal temperatures than liquid nitrogen cooled devices, will also increase the importance of such corrections.

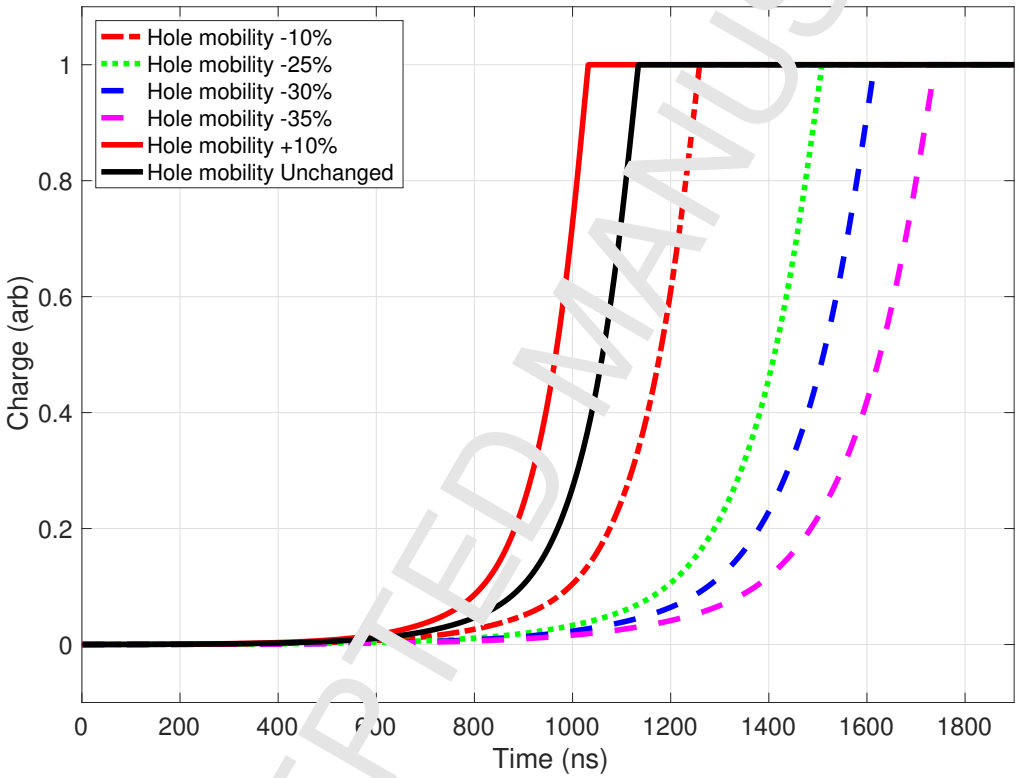

Figure 11: Simulated signals from point D4 using a range of values for the detector hole mobility in the <100> and <111> direction. The -30% shift is equivalent to that expected from a $T^{-2.3}$ relationship as temperature rises from 97.5 K to 113 K.

7. Acknowledgements

This research was supported by the United Kingdom Science and Technology Facilities Council (STFC UK) grant ST/N003543/1.

References

[1] M. T. (Canberra), Sage data sheet (2016).
URL http://canberra.com/products/detectors/pdf/SAGe-well-detector-SS-C49320.pdf

[2] R. Britton, A. Davies, Characterisation of a sage well detector using geant4 and labsocs, Nuclear Instruments and Methods in Physics Research Section A: Accelerators, Spectrometers, Detectors and Associated Equipment 786 (2015) 12 – 16. doi:https://doi.org/10.1016/j.nima.2015.03.036.
URL http://www.sciencedirect.com/science/article/pii/S0168900215003526

[3] A. S. Adekola, J. Colaresi, J. Douwen, H. Jderstrm, W. F. Mueller, K. M. Yocum, K. Carmichael, Characteristic performance evaluation of a new sage well detector for small and large sample geometries, IEEE Transactions on Nuclear Science 63 (3) (2016) 1570–1577. doi:10.1109/TNS.2015.2508676.

[4] B. Bruyneel, B. Birkenbach, P. Reiter, Pulse shape analysis and position determination in segmented hpge detectors: The agata detector library, The European Physical Journal A 52 (3) (2016) 70. doi:10.1140/epja/i2016-16070-9.
URL http://dx.doi.org/10.1140/epja/i2016-16070-9

[5] B. Bruyneel, P. Reiter, G. Pascovici, Characterization of large volume hpge detectors. part i: Electron and hole mobility parameterization, Nuclear Instruments and Methods in Physics Research Section A: Accelerators, Spectrometers, Detectors and Associated Equipment 569 (3) (2006) 764 –

773. doi:http://dx.doi.org/10.1016/j.nima.2006.08.130.
URL http://www.sciencedirect.com/science/article/pii/S0168900206015166

[6] W. Shockley, Currents to conductors induced by a moving point charge (1938), Journal of Applied Physics 9 (635). doi:http://dx.doi.org/10.1063/1.1710367.

[7] S. Ramo, Currents induced by electron motion (1939), Proceedings of the Institute of Radio Engineers.

[8] B. Bruyneel, P. Reiter, G. Pascovici, Characterization of large volume hpge detectors. part ii: Experimental results, Nuclear Instruments and Methods in Physics Research Section A: Accelerators, Spectrometers, Detectors and Associated Equipment 569 (3) (2006) 774 – 789. doi:http://dx.doi.org/10.1016/j.nima.2006.08.129.
URL http://www.sciencedirect.com/science/article/pii/S0168900206015178

[9] M. R. Dimmock, A. J. Boston, J. R. Cresswell, I. Lazarus, P. Medina, P. Nolan, C. Parisel, C. Santos, J. Simpson, C. Unsworth, Validation of Pulse Shape Simulations for an AGATA Prototype Detector, IEEE Transactions on Nuclear Science 56. doi:10.1109/TNS.2009.2021842.

[10] S. Akkoyun, A. Algora, B. Alikhani, F. Ameil, G. de Angelis, L. Arnold, A. Astier, A. Ataç, Y. Aubert, C. Aufranc, A. Austin, S. Aydin, F. Azaiez, S. Badoer, D. Balabanski, D. Barrientos, G. Baulieu, R. Baumann, D. Bazzacco, F. Beck, T. Beck, P. Bednarczyk, M. Bellato, M. Bentley, G. Benzoni, R. Berthier, L. Berti, R. Beunard, G. L. Bianco, B. Birkenbach, P. Bizzeti, A. Bizzeti-Sona, F. L. Blanc, J. Blasco, N. Blasi, D. Bloor, C. Boiano, M. Borsato, D. Bortolato, A. Boston, H. Boston, P. Bourgault, P. Boutachkov, A. Bouty, A. Bracco, S. Brambilla, I. Brawn, A. Brondi, S. Broussard, B. Bruyneel, D. Bucurescu, I. Burrows, A. Brger, S. Cabaret, B. Cahan, E. Calore, F. Camera, A. Capsoni, F. Carri,

G. Casati, M. Castoldi, B. Cederwall, J.-L. Cercus, V. Chambert, M. E. Chambit, R. Chapman, L. Charles, J. Chavas, E. Clement, P. Cocconi, S. Coelli, P. Coleman-Smith, A. Colombo, S. Colosimo, C. Commeaux, D. Conventi, R. Cooper, A. Corsi, A. Cortesi, L. Costa, F. Crespi, J. Cresswell, D. Cullen, D. Curien, A. Czermak, L. Delbourg, R. Depalo, T. Descombes, P. Dsesquelles, P. Detistov, C. Diarra, F. Didierjean, M. Dimmock, Q. Doan, C. Domingo-Pardo, M. Doncel, F. Dorangeville, N. Dosme, Y. Drouen, G. Duchne, B. Dulny, J. Eberth, P. Edelbruck, J. Egea, T. Engert, M. Erduran, S. Ertrk, C. Fanin, S. Fantinel, E. Farnea, T. Faul, M. Filliger, F. Filmer, C. Finck, G. de France, A. Gadea, W. Gast, A. Geraci, J. Gerl, R. Gernhuser, A. Giannatiempo, A. Giaz, L. Gibelin, A. Givechev, N. Goel, V. Gonzlez, A. Gottardo, X. Grave, J. Grebosz, R. Griffiths, A. Grint, P. Gros, L. Guevara, M. Gulmini, A. Grgen, H. Ha, T. Habermann, L. Harkness, H. Harroch, K. Hauschild, C. He, A. Hernndez-Prieto, B. Hervieu, H. Hess, T. Hyk, E. Ince, R. Isocrate, G. Jaworski, A. Johnson, J. Jolie, P. Jones, B. Jonson, P. Joshi, D. Judson, A. Jungclaus, M. Kaci, N. Karkour, M. Karolak, A. Kaka, M. Kebbiri, R. Kempley, A. Khaplanov, S. Klupp, M. Kogimtzis, I. Kojouharov, A. Korichi, W. Korten, T. Krll, R. Krcken, N. Kurz, B. Ky, M. Labiche, X. Lafay, L. Lavergne, I. Lazarus, S. Leboutelier, F. Lefebvre, E. Legay, L. Legeard, F. Lelli, S. Lenzi, S. Leoni, A. Lermitage, D. Lersch, J. Leske, S. Letts, S. Lhenoret, R. Lieder, D. Linget, J. Ljungvall, A. Lopez-Martens, A. Lotod, S. Lunardi, A. Maj, J. van der Marel, Y. Mariette, N. Marginean, R. Marginean, G. Maron, A. Mather, W. Meczyski, V. Mendez, P. Medina, B. Melon, R. Menegazzo, D. Mengoni, E. Merchan, P. Mihailescu, C. Michelagnoli, J. Mierzejewski, L. Milechina, B. Million, K. Mitev, P. Molini, D. Montanari, S. Moon, F. Morbiducci, R. Moro, P. Morrall, O. Mller, A. Nannini, D. Napoli, L. Nelson, M. Nespolo, V. Ngo, M. Nicoletto, R. Nicolini, Y. L. Noa, P. Nolan, M. Norman, J. Nyberg, A. Obertelli, A. Olariu, R. Orlandi, D. Oxley, C. zben, M. Ozille, C. Oziol, E. Pachoud, M. Palacz, J. Palin, J. Pancin, C. Parisel, P. Pariset, G. Pas-

covici, R. Peghin, L. Pellegri, A. Perego, S. Perrier, M. Petcu, P. Petkov, C. Petrache, E. Pierre, N. Pietralla, S. Pietri, M. Pignanelli, I. Piqueras, Z. Podolyak, P. L. Pouhalec, J. Pouthas, D. Pugnre, V. Pucknell, A. Pullia, B. Quintana, R. Raine, G. Rainovski, L. Ramina, G. Rampazzo, G. L. Rana, M. Rebeschini, F. Recchia, N. Redon, M. Reese, P. Reiter, P. Regan, S. Riboldi, M. Richer, M. Rigato, S. Rigby, G. Ripamonti, A. Robinson, J. Robin, J. Roccaz, J.-A. Ropert, B. Ross, C. R. Alvarez, D. Rosso, B. Rubio, D. Rudolph, F. Saillant, E. ahin, F. Salomon, M.-D. Salsac, J. Salt, G. Salvato, J. Sampson, E. Sanchis, C. Santos, H. Schaffner, M. Schlarb, D. Scraggs, D. Seddon, M. Seidlitz, M.-H. Sigward, G. Simpson, J. Simpson, M. Slee, J. Smith, P. Sona, P. Sowicki, P. Spolaore, C. Stahl, T. Stanios, E. Stefanova, O. Stezowski, J. Strachan, G. Suliman, P.-A. Sderstrm, J. Tain, S. Tanguy, S. Tashenov, C. Theisen, J. Thornhill, F. Tomasi, N. Toniolo, P. Touzery, B. Travers, A. Triossi, M. Tripon, K. Tun-Lano, M. Turcato, C. Unsworth, C. Ur, J. Valiente-Dobon, V. Vandone, E. Vardaci, R. Venturelli, F. Veronese, C. Veyssiere, E. Viscione, R. Wadsworth, P. Walker, J. Warr, C. Weber, D. Weisshaar, D. Wells, O. Wieland, A. Wiens, G. Wittwer, H. Wollersheim, F. Zocca, N. Zamfir, M. Ziebliski, A. Zucchiatti, Agataadvanced gamma tracking array, Nuclear Instruments and Methods in Physics Research Section A: Accelerators, Spectrometers, Detectors and Associated Equipment 668 (2012) 26 – 58. doi:https://doi.org/10.1016/j.nima.2011.11.081.
URI http://www.sciencedirect.com/science/article/pii/S0168900211021516

[11] L. Mihailescu, W. Gast, R. Lieder, H. Brands, H. Jger, The influence of anisotropic electron drift velocity on the signal shapes of closed-end {HPGe} detectors, Nuclear Instruments and Methods in Physics Research Section A: Accelerators, Spectrometers, Detectors and Associated Equipment 447 (3) (2000) 350 – 360. doi:http://dx.doi.org/10.1016/S0168-9002(99)01286-3.

URL http://www.sciencedirect.com/science/article/pii/S0168900299012863

[12] M. Schlarb, R. Gernhuser, S. Klupp, R. Krcken, Pulse shape analysis for -ray tracking (part i): Pulse shape simulation with jass, Eur. Phys. J. A 47 (10) (2011) 132. doi:10.1140/epja/i2011-11132-2.
URL https://doi.org/10.1140/epja/i2011-11132-2

[13] V. Prasher, M. Cromaz, E. Merchan, P. Chowdhury, H. Crawford, C. Lister, C. Campbell, I. Lee, A. Macchiavelli, D. Radford, A. Wiens, Sensitivity of gretina position resolution to hole mobility, Nuclear Instruments and Methods in Physics Research Section A: Accelerators, Spectrometers, Detectors and Associated Equipment 846 (2017) 50 – 55. doi:https://doi.org/10.1016/j.nima.2016.11.038.
URL http://www.sciencedirect.com/science/article/pii/S0168900216311925

[14] H. Hess, Private communication (2018).

[15] R. Lawrance, The temperature dependence of drift mobility in germanium, Phys. Rev. 89 (1953) 1295–1295. doi:10.1103/PhysRev.89.1295.
URL https://link.aps.org/doi/10.1103/PhysRev.89.1295

[16] M. B. Prince, Drift mobilities in semiconductors. i. germanium, Phys. Rev. 92 (1953) 681–687. doi:10.1103/PhysRev.92.681.
URL https://link.aps.org/doi/10.1103/PhysRev.92.681

[17] J. Wright, L. Harkness-Brennan, A. Boston, D. Judson, M. Labiche, J. Nolan, R. Page, F. Pearce, D. Radford, J. Simpson, C. Unsworth, Position resolution simulations for the inverted-coaxial germanium detector, sigma, Nuclear Instruments and Methods in Physics Research Section A: Accelerators, Spectrometers, Detectors and Associated Equipment 892 (2018) 84 – 92. doi:https://doi.org/10.1016/j.nima.2018.02.106.
URL http://www.sciencedirect.com/science/article/pii/S0168900218302948

[18] A. Domula, M. Hult, Y. Kermadic, G. Marissens, B. Schwingenheuer, T. Wester, K. Zuber, Pulse shape discrimination performance of inverted coaxial ge detectors, Nuclear Instruments and Methods in Physics Research Section A: Accelerators, Spectrometers, Detectors and Associated Equipmentdoi:https://doi.org/10.1016/j.nima.2018.02.056.
URL http://www.sciencedirect.com/science/article/pii/S0168900218302122